# Finite Source Properties of Large Strike-Slip Earthquakes

**James Atterholt**[1], **Zachary E. Ross**[1]

[1]California Institute of Technology

**Key Points:**

- We compute finite source properties for every large strike-slip earthquake of the past three decades in a probabilistic framework.
- With these source properties we show that most ruptures have either unilateral or a comparable mix of unilateral and bilateral directivity.
- We find that intraplate oceanic earthquakes are systematically deeper than other ruptures and are usually unaligned with fossil fractures.

Corresponding author: James Atterholt, `atterholt@caltech.edu`

## Abstract

Earthquake ruptures are complex physical processes that may vary with the structure and tectonics of the region in which they occur. Characterizing the factors controlling this variability would provide fundamental constraints on the physics of earthquakes and faults. We investigate this by determining finite source properties from second moments of the stress glut for a global dataset of large strike-slip earthquakes. Our approach uses a Bayesian inverse formulation with teleseismic body and surface waves, which yields a low-dimensional probabilistic description of rupture properties including spatial extent, directivity, and duration. This technique is useful for comparing events because it makes only minor geometric constraints, avoids bias due to rupture velocity parameterization, and yields a full ensemble of possible solutions given the uncertainties of the data. We apply this framework to all great strike-slip earthquakes of the past three decades, and we use the resultant second moments to compare source quantities like directivity ratio, rectilinearity, stress drop, and depth extent. We find that most strike-slip earthquakes have a large component of unilateral directivity, and many of these earthquakes show a mixture of unilateral and bilateral behavior. We also notice that oceanic intraplate earthquakes usually rupture a much larger width of the seismogenic zone than other strike-slip earthquakes, suggesting these earthquakes consistently breach the expected thermal boundary for oceanic ruptures. We also use these second moments to resolve nodal plane ambiguity for the large oceanic intraplate earthquakes and find that the rupture orientation is usually unaligned with encompassing fossil fracture zones.



## Plain Language Summary

Large strike-slip earthquakes present significant global hazard and provide unique windows into fundamental characteristics of the lithosphere. These earthquakes display a high degree of variability in behavior; discovering patterns in this variability may lead to a better understanding of these ruptures and the faults that host them. To this end, we determine several low-dimensional properties of all the large strike-slip earthquakes of the past three decades in a probabilistic framework. This approach allows us to compare these ruptures while considering the full range of potential rupture scenarios given the uncertainty of our data. We find that most of these ruptures either propagate unilaterally or exhibit a mix of bilateral and unilateral propagation behavior. We also observe that oceanic strike-slip earthquakes that rupture the interior of plates typically rupture deeper than expected. These intraplate oceanic earthquakes also appear to rupture independently of the encompassing fracture zones left over from the rifting process.

## 1 Introduction

Large earthquakes involve complex ruptures that can vary strongly between events. The characteristics of these ruptures may be controlled by the structural and tectonic characteristics of the fault zone, and understanding patterns in these ruptures may improve our understanding of the interplay between source phenomenology and the rupture zone. In particular, large strike-slip earthquakes are known to show considerable variability in rupture properties between events (e.g. Hayes, 2017; Yin et al., 2021; Bao et al., 2022). Systematically characterizing this variability has the potential to yield insights into the underlying controls on the rupture process. These insights are of societal and scientific interest because these earthquakes present significant global hazard and provide unique windows into the structure and rheology of the lithosphere. Several faults known to host large strike-slip earthquakes are in close proximity to dense population centers. There is also wide speculation that the propagation behavior and rupture dimensions are dictated by the structural (Ben-Zion & Andrews, 1998; Wesnousky, 2008) and rheological properties (Abercrombie & Ekström, 2001; Boettcher et al., 2007) of the host fault zone. Intraplate oceanic earthquakes are particularly enigmatic, because the explanation for the weakening of the oceanic lithosphere that accommodates these events remains elusive (Lay, 2019).

A general quantity for describing the space-time kinematics of earthquake ruptures is the so-called stress glut (G. Backus & Mulcahy, 1976a), which quantifies the breakdown of linear elasticity in space and time (Dahlen & Tromp, 1998). Finite-fault slip distributions, which approximate the stress glut as discretized slip on a predefined fault plane, are routinely computed for large events (Mai & Thingbaijam, 2014). These solutions provide a high dimensional view of fault ruptures but in practice are challenging to compare between events due to pervasive nonuniqueness in the inverse problem, a priori fault plane parameterization, poor rupture velocity sensitivity, and regularization. An alternative technique for characterizing earthquake source properties is the second-moment formulation (G. Backus & Mulcahy, 1976a,b). Instead of approximating the stress glut as a superposition of assigned subevents, this approach involves solving for the second order polynomial moments of the stress glut, yielding a source covariance matrix that approximates the spatiotemporal extent of the source. This technique has been successfully applied in the past (Bukchin, 1995; McGuire et al., 2000, 2001; McGuire, 2002, 2004; Chen, 2005; H. Meng et al., 2020), but has received far less attention than slip inversions. This low-dimensional framework makes only minor assumptions about rupture geometries and has the advantages of not requiring an explicitly paramaterized rupture velocity and avoiding the discretization challenges that arise when performing slip inversions. The low dimensionality of the solution also facilitates computation of these moments with a Bayesian approach (Atterholt & Ross, 2022), which can provide uncertainty estimates crucial for comparing the source processes of different earthquakes.

Our contributions to this study are as follows. We compute second moments for all of the $M_w \geq 7.5$ strike-slip earthquakes of the past three decades using a Bayesian inference approach. We use this catalog to establish baselines for the range of values observed globally and compare values between events, subgroups, and other tectonic features. From these analyses we conclude that (i) large strike-slip earthquakes almost always show unilateral or a comparable amount of unilateral and bilateral directivity behavior, (ii) that large intraplate oceanic earthquakes usually rupture over a much wider depth range, and (iii) that oceanic intraplate strike-slip earthquakes are not systematically aligned with fossil fracture zones.

## 2 Preliminaries

The stress glut is a tensor field representing the expected stress due to the application of Hooke's law to inelastic strain in a body (G. Backus & Mulcahy, 1976a,b). The

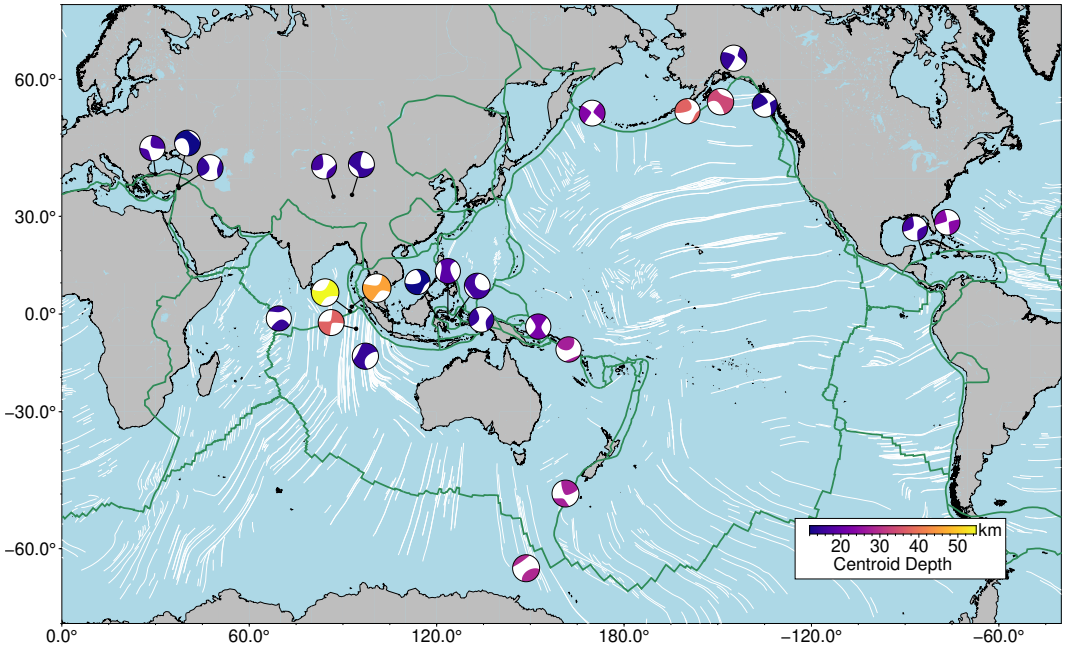


**Figure 1.** Centroid locations and centroid depths of the earthquakes used in this study. White lines are fossil fracture zone locations from (Seton et al., 2014; Wessel et al., 2015). Green lines are plate boundaries from (Bird, 2003).

stress glut is a useful source characterization quantity, because the stress glut is identically zero outside the source region and can be used to compute displacements anywhere on Earth resulting from an arbitrary source (Dahlen & Tromp, 1998). The dimensionality of the stress glut can be significantly reduced by assuming the source mechanism does not change throughout the rupture:

$$\Gamma_{ij}(\boldsymbol{\xi}, \tau) = \hat{M}_{ij} f(\boldsymbol{\xi}, \tau). \tag{1}$$

Here, $\boldsymbol{\Gamma}$ is the stress glut, $\hat{\mathbf{M}}$ is the normalized mean seismic moment tensor, and $f$ is a scalar function of position $\boldsymbol{\xi}$ and time $\tau$. The second moment formulation is defined by taking the second central moment of the scalar stress glut rate function ($\dot{f}$) with terms for the spatial and temporal components. The equation for these moments is given by:

$$\dot{f}(\boldsymbol{\xi}^c, \tau^c)^{(m,n)} = \int\int \dot{f}(\boldsymbol{\xi}, \tau)(\boldsymbol{\xi} - \boldsymbol{\xi}^c)^m (\tau - \tau^c)^n d\boldsymbol{\xi} d\tau, \tag{2}$$

where $\boldsymbol{\xi}$ and $\tau$ are position and time, $\boldsymbol{\xi}^c$ and $\tau^c$ are the centroid position and centroid time, and $m$ and $n$ are the spatial order and temporal order of the moment. The central moments of order $m + n = 2$ correspond to the covariance of the source. Specifically, $f(\boldsymbol{\xi}^c, \tau^c)^{(2,0)}$ is the spatial covariance, $f(\boldsymbol{\xi}^c, \tau^c)^{(0,2)}$ is the temporal variance, and $f(\boldsymbol{\xi}^c, \tau^c)^{(1,1)}$ is the spatiotemporal covariance. These moments can be linearly related to displacement:

$$\mathbf{d} = \mathbf{F}\mathbf{p} \tag{3}$$

Where $\mathbf{d}$ is a vector of the difference between the measured displacements and the theoretical Green's functions, $\mathbf{F}$ is a forward propagation matrix of spatial and temporal integrals and derivatives of the Green's tensor weighted by the components of the moment tensor $\mathbf{M}$, and $\mathbf{p}$ is a vector that contains the independent parameters of the second order stress-glut moments.

Since the standard deviation of a distribution gives a low-dimensional estimate of the width of a distribution, these second moments, which are the covariance of the stress-glut, can be used to compute low-dimensional measures of the volume, duration, and directivity of a source distribution. In particular, we define characteristic dimensions of the source that describe the shape of the stress-glut distribution about the centroid. These are:

$$\begin{aligned} r^c(\hat{\mathbf{n}}) &= \sqrt{\hat{\mathbf{n}}^{\mathbf{T}} \cdot [\dot{\boldsymbol{f}}^{(2,0)}(\boldsymbol{\xi}^c, \tau^c)/\dot{f}^{(0,0)}(\boldsymbol{\xi}^c, \tau^c)] \cdot \hat{\mathbf{n}}}, \\ t^c &= 2\sqrt{\dot{f}^{(0,2)}(\boldsymbol{\xi}^c, \tau^c)/\dot{f}^{(0,0)}(\boldsymbol{\xi}^c, \tau^c)}, \\ \mathbf{v_0} &= \dot{\boldsymbol{f}}^{(1,1)}(\boldsymbol{\xi}^c, \tau^c)/\dot{f}^{(0,2)}(\boldsymbol{\xi}^c, \tau^c) \end{aligned} \tag{4}$$

Here, $r^c(\hat{\mathbf{n}})$ is the distance from the centroid in the direction of a unit vector $\hat{n}$ that defines a characteristic ellipsoid in which most of the moment was released. The characteristic length of the source is given by $L^c = 2r^c(\boldsymbol{\eta})$, where $\boldsymbol{\eta}$ is the principal eigenvector of $\dot{\boldsymbol{f}}^{(2,0)}$. $t^c$ is a characteristic duration that captures a time interval in which most of the moment was released. $\mathbf{v_0}$ is the average instantaneous velocity of the rupture centroid. These quantities together provide a physically interpretable, low-dimensional estimate of a rupture's spatiotemporal behavior (G. E. Backus, 1977; Silver & Jordan, 1983).

Beyond computing characteristic dimensions, we can also compute ensembles of quantities from the characteristic dimensions that may further illuminate potential differences between ruptures. In particular, we inspect four derived parameters in this study: rectilinearity ($R$), directivity ratio ($\alpha$), stress drop ($\Delta\sigma$), and vertical extent ($Z$). We define these parameters as:

$$\begin{aligned} R &= 1 - \frac{\frac{1}{2}(\lambda_2 + \lambda_3)}{\lambda_1} \\ \alpha &= \frac{||\boldsymbol{v_0}||}{L^c t^c} \\ \Delta\sigma &= \frac{M_0}{(2)^3 \frac{4}{3}\pi\lambda_1\lambda_2\lambda_3} \\ Z &= 2\gamma_z r^c(\boldsymbol{\gamma}) \end{aligned} \tag{5}$$

Where $\lambda_1$, $\lambda_2$, and $\lambda_3$ are the eigenvalues of the spatial second moment, $M_0$ is the scalar moment of the rupture, and $\boldsymbol{\gamma}$ is the unit vector pointing in the direction with the maximum vertical component.

## 3 Methods

### 3.1 Data and Preprocessing

We use the Global Centroid Moment Tensor (gCMT) catalog to select large strike-slip earthquakes of the past three decades (Ekström et al., 2012). To find these events, we search the gCMT catalog for events with $M_w \geq 7.5$ and with nodal axis plunges greater than 45°. We then manually evaluate these events to ensure that each event shows predominantly strike-slip behavior, resulting in the set of events shown in Figure 1 and Table 1. We choose events of this magnitude because the frequency to which the waveforms

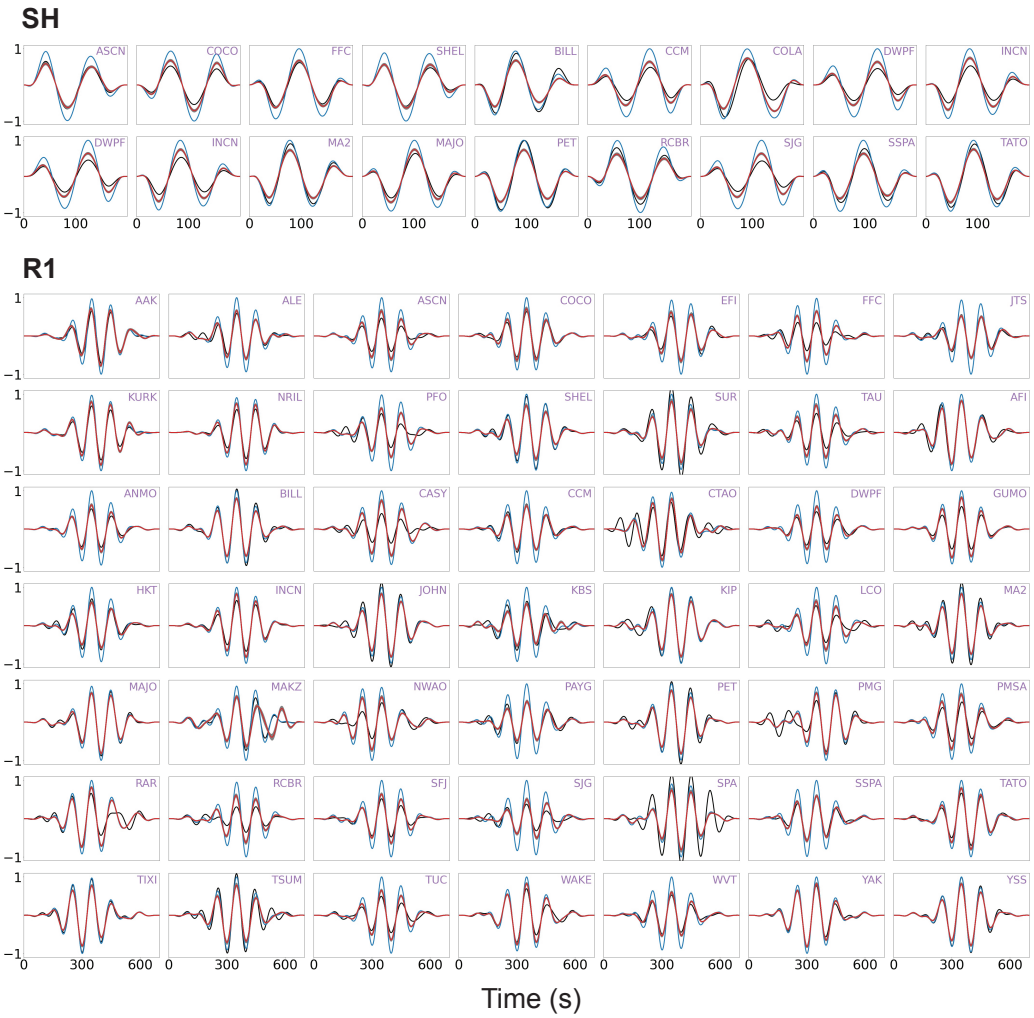


**Figure 2.** Examples of waveform fits for the 1999 $M_w$7.5 Izmit earthquake. The waveforms in the top grouping are fits to the SH phase. The waveforms in the bottom grouping are fits to the R1 phase. The black and blue lines correspond to the observed waveforms and the point source theoretical Green's functions at each respective station. The red and gray lines correspond to the waveform fit of the mean solution and the distribution of fits for the ensemble of solutions respectively.

**Table 1.** Global strike-slip earthquakes considered in this study. The values are drawn from the gCMT catalog (Ekström et al., 2012).

| Name | Date | Longitude | Latitude | Depth (km) | $M_w$ |
|---|---|---|---|---|---|
| Tibet | 1997-11-11 | 86.96 | 35.33 | 16.4 | 7.53 |
| Balleny Is. | 1999-03-25 | 148.64 | -62.99 | 28.8 | 8.14 |
| Ceram Sea | 1998-11-29 | 125.0 | -2.03 | 16.4 | 7.75 |
| Izmit | 1999-10-17 | 29,97 | 41.01 | 17.0 | 7.61 |
| Sulawesi | 2000-05-04 | 123.59 | -1.29 | 18.6 | 7.57 |
| Whar. Basin (1) | 2000-06-18 | 97.17 | -13.47 | 15.0 | 7.92 |
| Kunlun | 2001-11-14 | 92.91 | 35.8 | 15.0 | 7.81 |
| Irian Jaya | 2002-10-10 | 134.3 | -1.79 | 15.0 | 7.58 |
| Denali | 2002-11-03 | -144.89 | 63.23 | 15.0 | 7.88 |
| Carlsberg Rdg. | 2003-07-15 | 69.47 | -1.42 | 15.0 | 7.57 |
| Macquarie Is. | 2004-12-23 | 161.25 | -49.91 | 27.5 | 8.11 |
| Whar. Basin (2) | 2012-04-11 | 92.82 | 2.35 | 45.6 | 8.6 |
| Whar. Basin (3) | 2012-04-11 | 92.31 | 0.90 | 54.7 | 8.28 |
| S.E. of Alaska | 2013-01-05 | -134.97 | 55.69 | 13.8 | 7.56 |
| Solomon Is. | 2014-04-12 | 162.24 | -11.35 | 27.3 | 7.66 |
| Whar. Basin (4) | 2016-03-02 | 94.22 | -4.75 | 37.2 | 7.82 |
| Komandorski Is. | 2017-07-17 | 169.78 | 54.13 | 23.2 | 7.79 |
| Honduras | 2018-01-10 | -83.86 | 17.56 | 16.5 | 7.55 |
| Gulf of Alaska | 2018-01-23 | -149.12 | 56.22 | 33.6 | 7.96 |
| Palu | 2018-09-28 | 119.86 | -0.72 | 12.0 | 7.60 |
| Papua N.G. | 2019-05-14 | 152.52 | -4.03 | 22.1 | 7.60 |
| Canary Is. | 2020-01-28 | -79.55 | 19.33 | 23.9 | 7.72 |
| S. of Alaska | 2020-10-19 | -159.7 | 54.48 | 37.4 | 7.62 |
| Turkey-Syria (1) | 2023-02-06 | 37.47 | 37.56 | 14.9 | 7.83 |
| Turkey-Syria (2) | 2023-02-06 | 37.22 | 38.11 | 12.0 | 7.78 |

for these events need to be fit to resolve stress-glut second moments is inversely related to the duration of the event. Consequently, larger events with correspondingly larger durations may be fit with theoretical Green's functions at lower frequencies. We fit waveforms from the Global Seismographic Network (GSN) for data consistency between events. The waveforms used in these inversions are SH and R1 waveforms selected using travel times from the Preliminary Reference Earth Model (PREM) (Dziewonski & Anderson, 1981). The inclusion of the P waveforms would further constrain the posterior distributions, but we decide not to include these because their inclusion would require the computation of theoretical Green's functions at much higher frequencies. We select 200-second windows around the SH waveforms and 700-second windows around the R1 waveforms. Waveforms at distances less than 30 degrees are excluded to avoid the convolution of the SH waves with the R1 waves. An example set of waveforms for the 1999 Izmit earthquake are shown in Figure 2. We compute the Green's tensors using the gCMT moment tensor solutions (Ekström et al., 2012). We use the spectral element method software Salvus (Afanasiev et al., 2019) in combination with the 3D Earth model S362ANI+M (Moulik & Ekström, 2014) to compute the Green's tensors. The derivatives of the Green's functions needed for the forward propagation matrices are computed using a centered finite difference approximation. For the spatial finite difference, we compute the wavefield for a grid of source locations centered on the centroid solution.

As in Atterholt & Ross (2022), we select the frequency bands used in these inversions using duration estimates for each event. In particular, we consider the observation that the contribution of moments of order $m+n$ is approximately proportional to $(D/P)^{m+n}$ (where $(D/P) < 1$) (G. E. Backus, 1977). We select a frequency band such that $(D/P)^2 > 0.05$ and $(D/P)^3 < 0.05$ in order to balance maximizing the second moments relative to the zeroth and first moments while minimizing the contribution of moments of order three and greater. For an estimate of duration, we use the empirical relationship used for the gCMT catalog (Ekström et al., 2012). With the aforementioned inequality and duration estimates, we can compute a frequency band for filtering the data. Once filtered, we visually inspect the fit of the theoretical Green's functions to the data for quality control.

### 3.2 Inversion

For the second moment inversion, we follow the procedure outlined in Atterholt & Ross (2022), and we summarize the method here. In essence, our objective is to use the relationship described in equation 3 to invert for a model vector of stress glut moments that better fits displacement waveforms by accounting for the finiteness of the source. An example of the waveform fits for the 1999 Izmit earthquake using the subsequently-described inversion are shown in Figure 2.

We solve this inverse problem using a Bayesian formulation that produces an ensemble of potential solutions given the uncertainty of the inverse problem, outlined in detail by Atterholt & Ross (2022). The posterior distribution for this problem can be written using the relationship:

$$p(\mathbf{p}, \sigma|\mathbf{d}) \propto p(\mathbf{d}|\sigma, \mathbf{p})\; p(\sigma)\; p(\mathbf{p}), \tag{6}$$

Where $\sigma$ is a hyperparameter (Gelman et al., 2010). We compute the likelihood using a multivariate normal distribution:

$$p(\mathbf{d}|\sigma, \mathbf{p}) \propto \frac{1}{\sqrt{|\Sigma|}} \exp(-\frac{1}{2}(\mathbf{d} - \mathbf{F}\mathbf{p})^{\mathrm{T}}\, \mathbf{\Sigma}^{-1}\, (\mathbf{d} - \mathbf{F}\mathbf{p})) \tag{7}$$

Prior studies on stress-glut second moment inversions (Bukchin, 1995; McGuire et al., 2001) have applied the constraint that since second moments constitute a covariance matrix, only the solutions that ensure the second moments are positive definite are valid, or:

$$\mathbf{X} = \begin{bmatrix} \dot{\boldsymbol{f}}^{(2,0)}(\boldsymbol{\xi}^c, \tau^c) & \dot{\boldsymbol{f}}^{(1,1)}(\boldsymbol{\xi}^c, \tau^c) \\ \dot{\boldsymbol{f}}^{(1,1)}(\boldsymbol{\xi}^c, \tau^c)^T & \dot{f}^{(0,2)}(\boldsymbol{\xi}^c, \tau^c) \end{bmatrix} \succeq 0. \tag{8}$$

To ensure our samples of the posterior are positive definite, we take advantage of the Cholesky Factorization Theorem, which states that every symmetric, positive definite matrix can be represented as the product of a lower triangular matrix and its transpose. For $\mathbf{X}$, there thus exists a matrix $\mathbf{L}$ such that $\mathbf{X} = \mathbf{L}\mathbf{L}^T$. We thus sample over $\mathbf{L}$ and construct $\mathbf{X}$ from $\mathbf{L}$ when computing the likelihood of the sample.

## 4 Results and Discussion

### 4.1 Characteristic dimensions illuminate trends in rupture behavior

From our inversions we obtain ensembles of second moments for each event. Then using the definitions in Equation 4, we can subsequently compute ensembles of quantities that capture low dimensional rupture characteristics. We show the ensembles of these

parameters for each event in Figures S1, S2, and S3 and summarize them in Table 2. In Figure 3 we show projections of the ensembles of characteristic ellipsoids for a subset of the events used in this study. These characteristic ellipsoids are defined such that the axes are the principal components of the second spatial moments scaled by the standard deviation along that component. This is the equivalent of finding an ellipsoid that captures a single standard deviation of the source distribution in all directions. We selected these events for display here because there exist readily available fault slip distributions that were constrained using geodetic observations (Mai & Thingbaijam, 2014). We compute the expected spatial second moment characteristic ellipsoids for these fault slip distributions and compare them to our solutions as a verification of our inversion. As shown in Figure 3, there is fairly close agreement between our solutions and that of the fault slip distributions, especially given that we only use GSN teleseismic data in this study and impose no constraints on the fault plane. While it may seem that our ellipsoids are much wider in the fault normal direction than those computed from the slip distributions, this is in fact expected behavior; it is a consequence of the fact that the fault slip distributions parameterize slip on planar/curved surfaces rather than 3D volumes, resulting in spatial second moment ellipsoids that are artificially much narrower than they would be if the inversions were solved without this constraint.

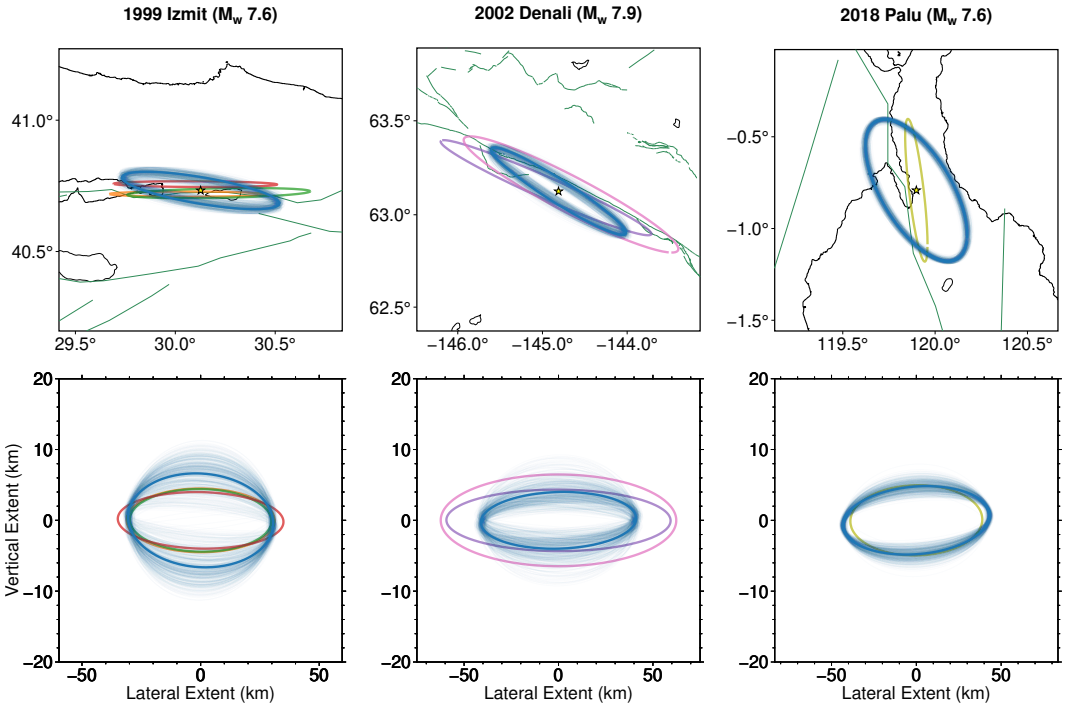


**Figure 3.** Map view (top row) and vertical plane (bottom row) projections of median (dark blue) and individual ensemble members (light blue) of spatial second moment ellipsoids for several events considered in this study. Other colored ellipsoid projections come from geodetically-constrained fault slip distributions reduced to the second moment form. Orange, green, red, purple, pink, and olive colored ellipsoids correspond to solutions from Çakir et al. (2003), Delouis (2002), Reilinger et al. (2000), Asano (2005), and Socquet et al. (2019) respectively.

In Figure 4 we plot the ensembles of characteristic durations, which show good agreement with the empirical magnitude-duration relationship used to determine the frequency bands used in this study. The initial duration estimates control the quality of the solution by reducing biases from the error of the moments of order $m + n \leq 1$ and from

the contributions of the moments of order $m+n \geq 3$, but this does not suggest a causal relationship between the initial duration estimates and the second temporal moments. These moments thus show that this empirical relationship is a reasonable model for these data.

Also shown in Figure 4 is a comparison between the characteristic length of the rupture, $L_c$, and the propagation length of the rupture centroid $||\boldsymbol{v}_0|| \cdot t^c$. The ratio between these two quantities reflects the degree of directivity of the rupture (McGuire, 2002). We separate these quantities into 3 categories of our design: bilateral ($||\boldsymbol{v}_0|| \cdot t^c / L_c \leq \frac{1}{3}$), mixed ($\frac{1}{3} \leq ||\boldsymbol{v}_0|| \cdot t^c / L_c \leq \frac{2}{3}$), and unilateral ($||\boldsymbol{v}_0|| \cdot t^c / L_c \geq \frac{2}{3}$). As is made clear in Figure 4, almost no ruptures fall in the bilateral category, suggesting that the vast majority of these ruptures have a large component of unilateral directivity, which is consistent with previous results (McGuire, 2002; Ross et al., 2020). But, while many of these ruptures fall in the unilateral category, suggesting these ruptures favor unilateral directivity over bilateral directivity, many of the ruptures also fall in the mixed category. Mixed directivity in ruptures may point to a more complicated rupture process. For example, rupture scenarios in which the initial propagation is bilateral, but the rupture is halted on one side earlier than the other side would produce a mixed directivity signal. These results show that scenarios like this are fairly common among large strike-slip events.

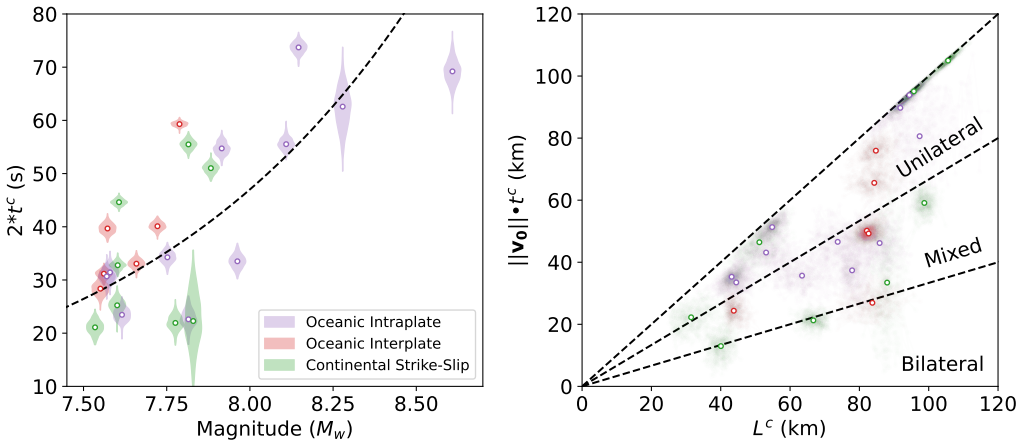


**Figure 4.** Left: Twice the characteristic duration ($\pm 2\sigma$ of moment rate function) for each event plotted against event moment magnitude. Black dotted line is the empirical magnitude-duration relationship used in (Ekström et al., 2012). Right: Characteristic length plotted against centroid propagation length. Black dotted lines separate bilateral, mixed, and unilateral categories described in the text. Green, red, and purple correspond to continental strike-slip, oceanic interplate, and oceanic intraplate respectively.

### 4.2 Derived source quantities suggest oceanic intraplate earthquakes have wider ruptures

We compute ensembles for the quantities described in Equation 5 for all the events considered in this study and plot them in Figure 5. Almost all rectilinearity values for these events are well-above 0.5, suggesting that most of these ruptures are elongated along a single dimension. Large strike-slip earthquakes are large-enough to be constrained by the width of the seismogenic zone, and thus elongation of the rupture ellipsoid in the strike-parallel direction is expected. The directivity ratio, also represented in Figure 4 and discussed in the previous section, yields a wide distribution that is biased towards values

closer to one. Stress drops for these events vary by over two orders of magnitude (1-100 MPa) with a median value near 10 MPa. The distribution of vertical extents is mostly below 20 km with a noteworthy tail extending up to 40 km. The ensembles of these parameters for each event are shown in Figures S1, S2, and S3 and are summarized in Table 2.

We separate these events into 3 categories: continental strike-slip, oceanic interplate, and oceanic intraplate. For oceanic events, we make classifications by cross-referencing the event locations with the plate boundary types outlined in Bird (2003). This classification is not always simple. For example, the 2003 Carlsberg Ridge event ruptured close to the active spreading center but with an opposite sense of slip as expected for the nearby transform faults. We nonetheless classified this event as interplate because of it's proximity to the plate boundary. We classify all continental strike-slip events together to ensure that there are enough events in the group to evaluate potential systematic behavior. The rectilinearity and directivity of these events are too variable within groups to make statements regarding differences between groups, but these ensembles demonstrate the potential of this second-moment framework to objectively obtain quantities that potentially illuminate rupture features that have historically been difficult to obtain. Some differences in stress drop are evident in these distributions; namely, the ensembles of stress drop for oceanic interplate earthquakes create a distribution that is much narrower than that of other strike-slip earthquakes, because the other types of events include the contributions of several earthquakes with ensembles of exceptionally high stress drop values.

The distributions of vertical extents of these events suggest a clear difference between oceanic intraplate earthquakes and other strike-slip earthquakes. The oceanic intraplate earthquakes exhibit much wider ruptures than other strike-slip earthquakes; this has been suspected before, particularly for Wharton Basin events (Aderhold & Abercrombie, 2016). The observations in this study provide some evidence for this difference globally. Mindful that the vertical extent measure only accounts for $\pm 1\sigma$ of the source distribution's vertical width, it is reasonable to expect that the source distribution extends over an even larger width than the estimated vertical extent of the rupture. Given that these intraplate oceanic earthquakes generally rupture colder lithosphere, some difference in vertical extent between rupture types is to be expected. For earthquakes that ruptured oceanic crust with measured age, we can account for the expected thermal differences by comparing the age of the oceanic crust encompassing the centroid, taken from Seton et al. (2020), to the expected thermal profile of a half space cooling model with an ambient mantle temperature of 1350° and thermal diffusivity of $10^6 \mathrm{m}^2/\mathrm{s}$ as in Aderhold & Abercrombie (2016). Noting that the vertical extents are estimates of the variance of the stress glut from the centroid, we can estimate the depth extent of these earthquakes by summing the centroid depth with quantities proportional to the vertical extent of the source.

We plot these distributions of depth extent assuming the depth extents given by the conservative estimates of $\boldsymbol{\xi}^c(z)+\frac{1}{2}VE$ and $\boldsymbol{\xi}^c(z)+\frac{\sqrt{2}}{2}VE$ in Figure 6. The $\boldsymbol{\xi}^c(z)+\frac{1}{2}VE$ values assume slip only occurred within a single standard deviation of the source distribution below the source centroid, and the $\boldsymbol{\xi}^c(z)+\frac{\sqrt{2}}{2}VE$ values would yield the exact depth extents for source distributions with uniform slip. As is apparent in Figure 6, for interplate events these values consistently fall above the 800° isotherm and for intraplate events these values consistently fall below the 800° isotherm. While there is some variability in estimates of the limiting temperature for slip on oceanic transform faults (e.g Wiens & Stein, 1983; Abercrombie & Ekström, 2001), the estimates of depth extent of the slip for oceanic intraplate earthquakes frequently exceed even the highest expected slip-limiting temperatures. This motivates the consideration of a mechanism for coseismic slip below the brittle-ductile transition zone for large intraplate earthquakes. One potential mechanism for such a large amount of moment released below the brittle-ductile

transition zone, proposed as an explanation for the slip in 2012 Wharton Basin Earthquake, is a large component of deep viscous failure, rather than frictional failure, resulting from a runaway feedback system due to heating of the shear zone (Kelemen & Hirth, 2007; McGuire & Beroza, 2012). This mechanism, however, would only account for moment released between 600° and 800°. Another potential explanation is that diffuse deformation zones in the interior of oceanic lithosphere may be hydrated at depth, altering the rheological profile of the fault (Bishop et al., 2023) and thus allowing for deeper rupture. Regardless of the mechanism, these results suggest that this behavior is nearly systematic for events of this type.

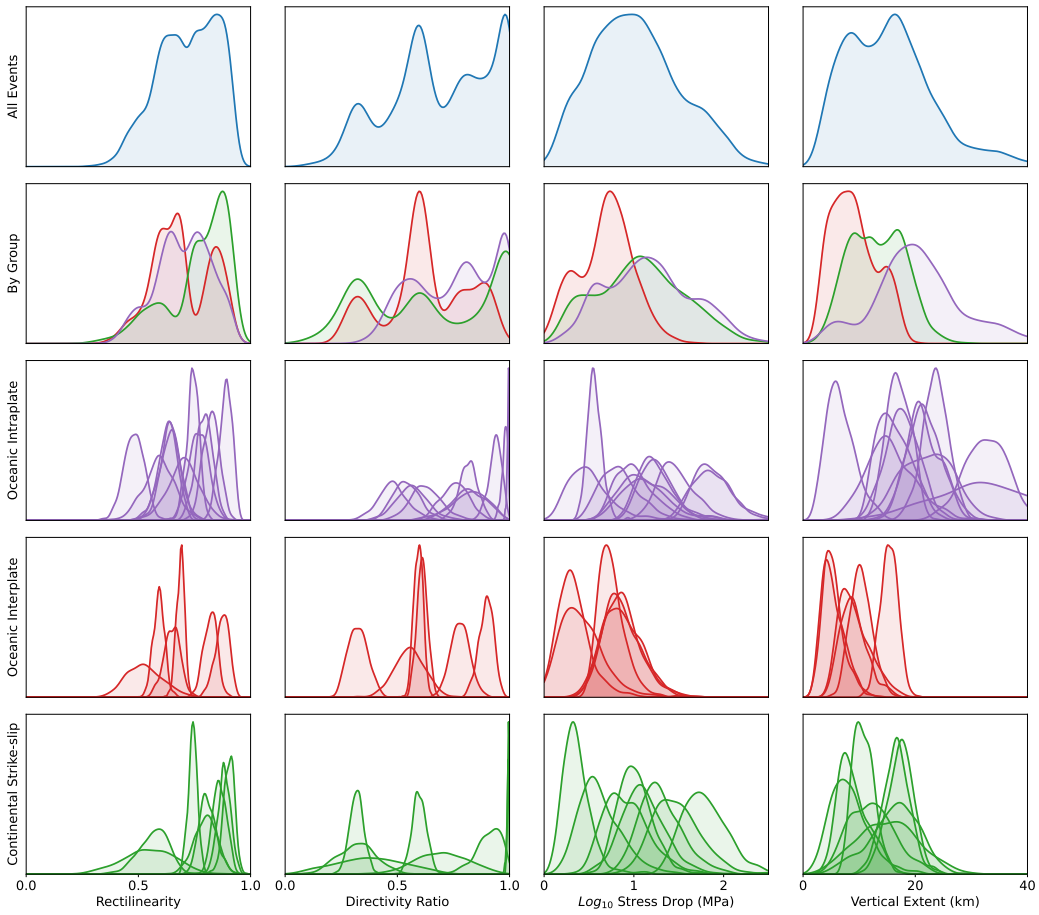


**Figure 5.** Derived source quantities described in the text. Top row: Distributions of all event ensembles for each quantity. Second row from the top: Distributions of all ensembles within individual tectonic groups for each quantity. Green, red, and purple correspond to continental strike-slip, oceanic interplate, and oceanic intraplate respectively. Bottom three rows: ensemble distributions for individual events within each tectonic category for each quantity. The relative heights of a few distributions of directivity ratio for individual sources were were reduced for visualization purposes.

**Table 2.** Ensembles of parameters defined in Equations 4 and 5 summarized for the events in this study. For each parameter, the median value and a credible interval ($5^{\text{th}}$ to $95^{\text{th}}$ percentile) are given.

| Name | $L_c$ (km) | $\|\|\boldsymbol{v_0}\|\|$ (km/s) | $t_c$ (s) | $R$ | $\alpha$ | $Log(\Delta\sigma)$ (MPa) | $Z$ (km) |
|---|---|---|---|---|---|---|---|
| Tibet | 51.1 (45.4-57.9) | 4.39 (3.54-5.51) | 10.6 (9.5-11.6) | 1.1 (0.9-1.3) | 0.91 (0.79-0.98) | 0.58 (0.3-1.1) | 7.7 (3.5-13.7) |
| Balleny Is. | 94.4 (90.4-98.9) | 2.55 (2.43-2.69) | 36.86 (35.9-37.6) | 1.5 (1.4-1.6) | 0.99 (0.98-1.0) | 1.25 (1.0-1.7) | 15.9 (12.0-21.8) |
| Ceram Sea | 44.5 (39.6-48.9) | 1.96 (1.73-2.19) | 17.1 (16.2-18.0) | 1.3 (1.1-1.4) | 0.76 (0.66-0.86) | 1.21 (1.0-1.6) | 21.2 (16.9-27.2) |
| Izmit | 66.7 (63.0-70.4) | 0.95 (0.81-1.1) | 22.3 (21.8-22.8) | 1.6 (1.5-1.8) | 0.32 (0.27-0.37) | 1.0 (0.7-1.3) | 16.7 (8.2-22.7) |
| Sulawesi | 77.9 (75.4-81.9) | 2.42 (1.84-3.22) | 15.34 (14.3-16.3) | 1.8 (1.7-1.9) | 0.48 (0.37-0.59) | 1.12 (0.8-1.7) | 6.3 (3.1-11.7) |
| Whar. Basin (1) | 85.8 (80.0-91.5) | 1.68 (1.41-2.0) | 27.4 (26.5-28.3) | 1.6 (1.5-1.7) | 0.54 (0.45-0.64) | 0.98 (0.7-1.4) | 15.2 (9.0-24.1) |
| Kunlun | 105.6 (102.1-109.0) | 3.79 (3.61-3.97) | 27.7 (27.0-28.5) | 1.7 (1.6-1.8) | 0.99 (0.99-1.0) | 0.89 (0.6-1.4) | 15.2 (6.7-24.3) |
| Irian Jaya | 63.5 (56.0-72.2) | 2.25 (1.89-2.73) | 15.7 (14.7-16.7) | 1.3 (1.1-1.4) | 0.56 (0.46-0.69) | 0.47 (0.2-0.9) | 17.7 (12.9-22.6) |
| Denali | 95.7 (91.9-100.1) | 3.73 (3.49-3.97) | 25.5 (24.7-26.2) | 1.8 (1.7-1.9) | 0.99 (0.98-1.0) | 1.26 (1.0-1.8) | 8.4 (5.6-14.5) |
| Carlsberg Rdg. | 84.3 (78.3-90.4) | 3.31 (3.06-3.6) | 19.8 (19.1-20.6) | 1.3 (1.2-1.4) | 0.78 (0.71-0.85) | 0.31 (0.1-0.7) | 10.2 (7.4-13.7) |
| Macquarie Is. | 53.1 (46.1-59.7) | 1.55 (1.39-1.75) | 27.8 (27.0-28.7) | 1.2 (1.0-1.4) | 0.82 (0.7-0.94) | 1.45 (1.2-1.9) | 22.3 (15.0-29.5) |
| Whar. Basin (2) | 91.8 (85.2-98.0) | 2.6 (2.39-2.84) | 34.6 (32.8-36.5) | 1.5 (1.4-1.7) | 0.98 (0.95-1.0) | 1.85 (1.6-2.2) | 32.7 (26.2-39.0) |
| Whar. Basin (3) | 97.4 (90.8-109.2) | 2.58 (2.12-3.06) | 31.3 (28.0-34.1) | 1.4 (1.2-1.6) | 0.83 (0.67-0.94) | 1.07 (0.7-1.6) | 32.1 (17.4-47.5) |
| S.E. of Alaska | 82.2 (78.8-86.4) | 3.22 (2.96-3.55) | 15.6 (14.9-16.1) | 1.2 (1.1-1.3) | 0.61 (0.57-0.65) | 0.38 (0.1-0.8) | 5.0 (2.6-9.2) |
| Solomon Is. | 43.8 (41.7-47.5) | 1.48 (1.21-1.75) | 16.5 (15.8-17.2) | 1.0 (0.8-1.3) | 0.55 (0.45-0.66) | 0.73 (0.6-1.0) | 15.3 (12.8-17.8) |
| Whar. Basin (4) | 73.7 (67.5-83.1) | 4.08 (3.37-5.01) | 11.3 (10.0-12.8) | 1.3 (1.1-1.4) | 0.63 (0.52-0.75) | 0.83 (0.5-1.2) | 21.5 (17.1-26.5) |
| Komandorski Is. | 82.7 (80.6-86.0) | 1.66 (1.57-1.75) | 29.7 (29.3-30.0) | 1.4 (1.3-1.4) | 0.59 (0.56-0.63) | 0.84 (0.6-1.2) | 5.1 (2.8-9.1) |
| Honduras | 83.7 (75.4-90.2) | 1.89 (1.47-2.42) | 14.2 (13.2-15.2) | 1.8 (1.6-1.8) | 0.32 (0.26-0.4) | 0.84 (0.5-1.3) | 9.1 (5.8-14.7) |
| Gulf of Alaska | 54.8 (51.6-58.4) | 3.07 (2.77-3.42) | 16.8 (15.7-17.8) | 1.7 (1.5-1.8) | 0.94 (0.88-0.98) | 1.86 (1.6-2.3) | 16.9 (13.6-20.5) |
| Palu | 98.7 (96.0-101.6) | 3.61 (3.21-4.01) | 16.4 (15.7-17.0) | 1.5 (1.4-1.5) | 0.6 (0.55-0.65) | 0.34 (0.2-0.6) | 10.6 (8.1-14.2) |
| Papua N.G. | 31.5 (26.5-38.5) | 1.75 (1.3-2.25) | 12.6 (11.5-13.6) | 1.1 (0.7-1.4) | 0.7 (0.51-0.88) | 1.09 (0.8-1.5) | 12.1 (6.5-19.9) |
| Canary Is. | 84.8 (80.8-89.6) | 3.78 (3.48-4.1) | 20.1 (19.4-20.7) | 1.6 (1.5-1.7) | 0.9 (0.84-0.94) | 0.86 (0.6-1.2) | 8.4 (5.5-13.6) |
| S. of Alaska | 43.1 (40.4-46.3) | 3.0 (2.61-3.45) | 11.7 (10.8-12.7) | 1.0 (0.8-1.1) | 0.82 (0.75-0.88) | 0.56 (0.4-0.7) | 23.6 (19.5-27.3) |
| Turkey-Syria (1) | 88.0 (84.2-92.1) | 2.89 (0.93-6.56) | 11.1 (7.0-15.2) | 1.8 (1.7-1.9) | 0.38 (0.13-0.63) | 1.46 (1.1-2.0) | 16.7 (12.7-20.5) |
| Turkey-Syria (2) | 40.0 (36.5-43.6) | 1.17 (0.65-1.69) | 11.0 (9.8-12.1) | 1.6 (1.4-1.8) | 0.32 (0.18-0.46) | 1.77 (1.4-2.2) | 17.5 (13.4-21.0) |

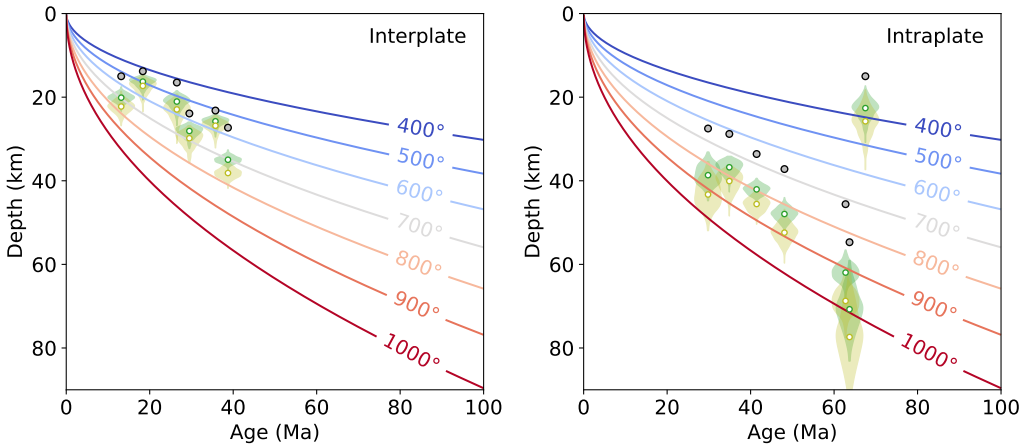


**Figure 6.** Depth extent of earthquakes plotted against lithospheric age. Isotherms generated using a half-space cooling model with an ambient mantle temperature of 1350°. Gray points are the gCMT centroid depths. Green violin plots are distributions of depth extents estimated by $\boldsymbol{\xi}^c(z) + \frac{1}{2}VE$. Yellow violin plots are depth extents estimated by $\boldsymbol{\xi}^c(z) + \frac{\sqrt{2}}{2}VE$. Left and right figures includes all interplate and intraplate events included in this study for which oceanic lithosphere age was obtainable respectively. Lithospheric age is obtained from Seton et al. (2020).

### 4.3 Oceanic intraplate earthquake rupture orientation does not correlate with fossil fracture zone strike

For large strike-slip earthquakes that occur on plate boundaries or in continental crust, the fault associated with the majority of slip is typically well resolved or easy to infer from the focal mechanism. However, for intraplate oceanic earthquakes, the true fault plane is often not easily resolved (e.g. Nettles et al., 1999; Abercrombie et al., 2003; Robinson, 2011; L. Meng et al., 2012; Lay et al., 2018). The determination of the primary fault plane for these earthquakes (if one exists) is an important problem, because the enigmatic rupture of these very large events may broaden our understanding of the strength of the oceanic lithosphere and the nature of these earthquakes. A frequent assumption is that these events rupture fossil fracture zones, crustal fabric imparted by ocean spreading. However, some detailed studies of several events suggest rupture plane strikes that disagree with those of nearby fracture zones or rupture several nearly-orthogonal fault planes (Nettles et al., 1999; L. Meng et al., 2012; Lay et al., 2018), making the fracture zone hypothesis an unlikely universal explanation for weakening of the oceanic lithosphere. This motivates a systematic analysis of how often these large events align with fossil fracture zones. Historically, this has not been straightforward because of the nodal plane ambiguity of the moment tensor solution and the lack of near source instrumentation for these special events.

The second moment formulation can be used to resolve the nodal plane ambiguity of a point source moment tensor solution. Since we expect the slip variance to be maximized along the rupture plane, the principal eigenvector of the spatial second moment should be approximately aligned with the strike of the true nodal plane. We can verify this by comparing the strike of the principal eigenvectors of the ensembles of second spatial moments with true nodal plane of earthquakes for which this can be easily inferred. For all continental strike-slip earthquakes and interplate oceanic events, we can be reasonably confident of the true nodal plane in the presence of an observed surface rupture or nearby plate boundary information. For each of these events, we plot (Fig. 7) the dif-

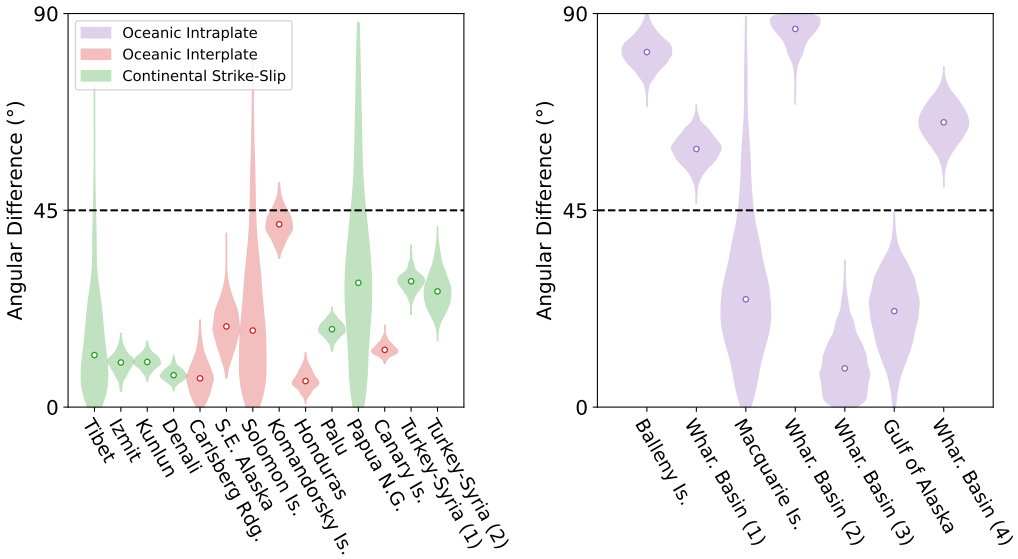


**Figure 7.** Left: Comparison of principal eigenvector strike ensembles with true nodal plane strikes for all continental strike-slip and interplate oceanic earthquakes. Right: Comparison of principal eigenvector strike ensembles with fracture zone strike estimation described in the main text for intraplate oceanic earthquakes near mapped fossil fracture zones. For both plots, black, brown, and gray dotted lines correspond to 0°, 45°, and 90° differences respectively. Green, red, and purple correspond to continental strike-slip, oceanic interplate, and oceanic intraplate respectively.

ference in angle between the strike of the inferred nodal plane and the strike of the principal eigenvectors for the corresponding ensemble of spatial second moments. The median and vast majority of the angular differences of each ensemble are less than 45°, suggesting that this methodology is an effective tool for approximating the strike of the true rupture plane.

An important point about this technique should be made here. Intraplate oceanic ruptures have been observed to rupture multiple, near-orthogonal faults throughout the course of the rupture (L. Meng et al., 2012; Lay et al., 2018). For these ruptures, the source mechanism remains approximately constant because the rupturing faults are nearly orthogonal, and thus the geometric assumption of this methodology remains valid. The stress glut covariance will track the distribution of moment release throughout the course of the rupture, and so for multi-fault ruptures the principal eigenvector may be unaligned with the rupture planes. For an intraplate oceanic earthquake, if this results in the principal eigenvector being unaligned with fossil fracture zones, we consider this a valid example of crustal weakening resulting in rupture that cannot be explained solely by fossil fracture zones, because such a rupture necessarily propagates on multiple faults, some of which will be oriented at high angle to local fossil fractures.

We apply this technique to the intraplate oceanic earthquakes that are situated near mapped fracture zones. We estimate the fracture zone strike in the area by considering the strikes of the fracture zones within 2° the event centroid. We compute fracture strikes using the shapefiles provided by Seton et al. (2014) and Wessel et al. (2015). For each event, we take the angular difference between the entire ensemble of principal eigenvectors and every potential fracture strike to create a distribution of potential angular dif-

ferences. We plot these distributions in Figure 7. We find that only 3 of the 7 distributions have any members within 45° of the fracture zone strike, suggesting that, more often than not, these ruptures are unaligned with the surrounding ocean fabric. Indeed, this methodology cannot decisively say whether or not the ruptures with principal eigenvectors that fall within 45° of the fracture zone strike actually ruptured the fracture zone, but the large disagreement between principal eigenvector strike and fracture zone strike for the other ruptures suggest that it is very unlikely that fossil fracture zones dictated the primary rupture plane. This motivates new explanations for weakening in the interior of the oceanic lithosphere that could host these large events, such as the explanation that diffuse deformation away from the plate boundary may induce faulting independent of preexisting ocean fabric.

## 5 Conclusions

By computing ensembles of stress glut second moments for all large strike-slip earthquakes of the past few decades, we illuminated several patterns in these ruptures that suggest predominant behaviors and variability with tectonic environment. Our results show that large strike-slip ruptures usually have a large component of unilateral behavior, with many ruptures exhibiting evidence for complicated rupture propagation sequences. We also observed that intraplate oceanic events have systematically wider ruptures than other large strike-slip earthquakes, potentially illustrating a systematic behavior of rupturing below the expected brittle-ductile transition zone depth. Finally, we show that by resolving the approximate rupture plane strike of major oceanic intraplate earthquakes, most of the earthquakes show no alignment with the fossil fracture zones in the area. This suggests that the assumption that large oceanic intraplate earthquakes reactivate fossil fracture zones is usually incorrect.

## 6 Open Research

The map shown in Figure 1 was created using The Generic Mapping Tools (GMT), version 6 (Wessel et al., 2019), which is available at https://www.generic-mapping-tools.org/. The centroid moment tensor solutions used in this study are from the Global Centroid Moment Tensor (gCMT) catalog (Ekström et al., 2012) which is accessible online at https://www.globalcmt.org/. The theoretical Green's functions were computed using Salvus (Afanasiev et al., 2019), which is available at https://mondaic.com/. The waveform data in this study are from the Global Seismographic Network operated by both the Albuquerque Seismological Laboratory (IU: IRIS/USGS; https://doi.org/10.7914/SN/IU) (Albuquerque Seismological Laboratory (ASL)/USGS, 1988) and the Scripps Institution of Oceanography (II: IRIS/IDA; https://doi.org/10.7914/SN/II) (Scripps Institution Of Oceanography, 1986). These waveforms may be accessed through the IRIS Data Management Center (DMC).

**Acknowledgments**
This work was partially funded by the National Science Foundation's Graduate Research Fellowship Program (GRFP) with grant number DGE-1745301. The authors would like to thank Dr. Joann Stock for her insightful comments and suggestions regarding intraplate oceanic ruptures.

## References

Abercrombie, R. E., Antolik, M., & Ekström, G. (2003, January). The June 2000 $M_w$ 7.9 earthquakes south of Sumatra: Deformation in the India-Australia Plate: THE JUNE 2000 INDIAN OCEAN EARTHQUAKES. *Journal of Geophysical Research: Solid Earth*, *108*(B1), ESE 6–1–ESE 6–16. Retrieved 2023-01-18, from http://doi.wiley.com/10.1029/2001JB000674 doi: 10.1029/2001JB000674

Abercrombie, R. E., & Ekström, G. (2001, March). Earthquake slip on oceanic transform faults. *Nature*, *410*(6824), 74–77. Retrieved 2023-01-13, from http://www.nature.com/articles/35065064 doi: 10.1038/35065064

Aderhold, K., & Abercrombie, R. E. (2016, May). Seismotectonics of a diffuse plate boundary: Observations off the Sumatra-Andaman trench. *Journal of Geophysical Research: Solid Earth*, *121*(5), 3462–3478. Retrieved 2023-01-19, from https://onlinelibrary.wiley.com/doi/10.1002/2015JB012721 doi: 10.1002/2015JB012721

Afanasiev, M., Boehm, C., van Driel, M., Krischer, L., Rietmann, M., May, D. A., ... Fichtner, A. (2019). Modular and flexible spectral-element waveform modelling in two and three dimensions. *Geophysical Journal International*, *216*(3), 1675-1692. doi: 10.1093/gji/ggy469

Albuquerque Seismological Laboratory (ASL)/USGS. (1988). *Global Seismograph Network (GSN - IRIS/USGS).* International Federation of Digital Seismograph Networks. Retrieved from http://www.fdsn.org/doi/10.7914/SN/IU doi: 10.7914/SN/IU

Asano, K. (2005, October). Estimation of Source Rupture Process and Strong Ground Motion Simulation of the 2002 Denali, Alaska, Earthquake. *Bulletin of the Seismological Society of America*, *95*(5), 1701–1715. Retrieved 2022-07-05, from https://pubs.geoscienceworld.org/bssa/article/95/5/1701-1715/103172 doi: 10.1785/0120040154

Atterholt, J., & Ross, Z. E. (2022, April). Bayesian Framework for Inversion of Second-Order Stress Glut Moments: Application to the 2019 Ridgecrest Sequence Mainshock. *Journal of Geophysical Research: Solid Earth*, *127*(4). Retrieved 2022-06-21, from https://onlinelibrary.wiley.com/doi/10.1029/2021JB023780 doi: 10.1029/2021JB023780

Backus, G., & Mulcahy, M. (1976a, August). Moment tensors and other phenomenological descriptions of seismic sources–I. Continuous displacements. *Geophysical Journal International*, *46*(2), 341–361. Retrieved 2020-11-05, from https://academic.oup.com/gji/article-lookup/doi/10.1111/j.1365-246X.1976.tb04162.x doi: 10.1111/j.1365-246X.1976.tb04162.x

Backus, G., & Mulcahy, M. (1976b, November). Moment tensors and other phenomenological descriptions of seismic sources–II. Discontinuous displacements. *Geophysical Journal International*, *47*(2), 301–329. Retrieved 2020-11-05, from https://academic.oup.com/gji/article-lookup/doi/10.1111/j.1365-246X.1976.tb01275.x doi: 10.1111/j.1365-246X.1976.tb01275.x

Backus, G. E. (1977, October). Interpreting the seismic glut moments of total degree two or less. *Geophysical Journal International*, *51*(1), 1–25. Retrieved 2020-11-05, from https://academic.oup.com/gji/article-lookup/doi/10.1111/j.1365-246X.1977.tb04187.x doi: 10.1111/j.1365-246X.1977.tb04187.x

Bao, H., Xu, L., Meng, L., Ampuero, J.-P., Gao, L., & Zhang, H. (2022, November). Global frequency of oceanic and continental supershear earthquakes. *Nature Geoscience*, *15*(11), 942–949. Retrieved 2023-01-13, from https://www.nature.com/articles/s41561-022-01055-5 doi: 10.1038/s41561-022-01055-5

Ben-Zion, Y., & Andrews, D. J. (1998, August). Properties and implications of dynamic rupture along a material interface. *Bulletin of the Seismological Society of America*, *88*(4), 1085–1094. Retrieved 2022-01-13, from https://pubs.geoscienceworld.org/bssa/article/88/4/1085/120342/Properties-and-implications-of-dynamic-rupture doi: 10.1785/BSSA0880041085

Bird, P. (2003, March). An updated digital model of plate boundaries. *Geochemistry, Geophysics, Geosystems*, *4*(3), 297–356. Retrieved 2021-06-20, from http://doi.wiley.com/10.1029/2001GC000252 doi: 10.1029/2001GC000252

Bishop, B. T., Cho, S., Warren, L., Soto-Cordero, L., Pedraza, P., Prieto, G. A., & Dionicio, V. (2023, February). Oceanic intraplate faulting as a pathway for deep

hydration of the lithosphere: Perspectives from the Caribbean. *Geosphere*, *19*(1), 206–234. Retrieved 2023-02-16, from https://pubs.geoscienceworld.org/geosphere/article/19/1/206/619073/Oceanic-intraplate-faulting-as-a-pathway-for-deep doi: 10.1130/GES02534.1

Boettcher, M. S., Hirth, G., & Evans, B. (2007, January). Olivine friction at the base of oceanic seismogenic zones. *Journal of Geophysical Research*, *112*(B1), B01205. Retrieved 2023-01-13, from http://doi.wiley.com/10.1029/2006JB004301 doi: 10.1029/2006JB004301

Bukchin, B. (1995, August). Determination of stress glut moments of total degree 2 from teleseismic surface wave amplitude spectra. *Tectonophysics*, *248*(3-4), 185–191. Retrieved 2020-11-05, from https://linkinghub.elsevier.com/retrieve/pii/004019519400271A doi: 10.1016/0040-1951(94)00271-A

Chen, P. (2005, June). Finite-moment tensor of the 3 September 2002 Yorba Linda Earthquake. *Bulletin of the Seismological Society of America*, *95*(3), 1170–1180. Retrieved 2020-11-05, from https://pubs.geoscienceworld.org/bssa/article/95/3/1170-1180/103154 doi: 10.1785/0120040094

Dahlen, F., & Tromp, J. (1998). *Theoretical global seismology.* Princeton, N.J.: Princeton University Press.

Delouis, B. (2002, February). Joint Inversion of InSAR, GPS, Teleseismic, and Strong-Motion Data for the Spatial and Temporal Distribution of Earthquake Slip: Application to the 1999 Izmit Mainshock. *Bulletin of the Seismological Society of America*, *92*(1), 278–299. Retrieved 2023-01-19, from https://pubs.geoscienceworld.org/bssa/article/92/1/278-299/102952 doi: 10.1785/0120000806

Dziewonski, A. M., & Anderson, D. L. (1981). Preliminary reference earth model. *Geophysical Journal International*, *25*, 297–356.

Ekström, G., Nettles, M., & Dziewoński, A. (2012, June). The global CMT project 2004–2010: Centroid-moment tensors for 13,017 earthquakes. *Physics of the Earth and Planetary Interiors*, *200-201*, 1–9. Retrieved 2020-11-05, from https://linkinghub.elsevier.com/retrieve/pii/S0031920112000696 doi: 10.1016/j.pepi.2012.04.002

Gelman, A., Carlin, J., Stern, H., Dunson, D., Vehtari, A., & Rubin, D. (2010). *Bayesian data analysis.* Boca Raton, F.L.: Chapman and Hall-CRC Press.

Hayes, G. P. (2017, June). The finite, kinematic rupture properties of great-sized earthquakes since 1990. *Earth and Planetary Science Letters*, *468*, 94–100. Retrieved 2023-01-13, from https://linkinghub.elsevier.com/retrieve/pii/S0012821X17301826 doi: 10.1016/j.epsl.2017.04.003

Kelemen, P. B., & Hirth, G. (2007, April). A periodic shear-heating mechanism for intermediate-depth earthquakes in the mantle. *Nature*, *446*(7137), 787–790. Retrieved 2023-01-18, from http://www.nature.com/articles/nature05717 doi: 10.1038/nature05717

Lay, T. (2019). Reactivation of Oceanic Fracture Zones in Large Intraplate Earthquakes? In *Transform Plate Boundaries and Fracture Zones* (pp. 89–104). Elsevier. Retrieved 2023-01-13, from https://linkinghub.elsevier.com/retrieve/pii/B9780128120644000049 doi: 10.1016/B978-0-12-812064-4.00004-9

Lay, T., Ye, L., Bai, Y., Cheung, K. F., & Kanamori, H. (2018, September). The 2018  $M_w$  7.9 Gulf of Alaska Earthquake: Multiple Fault Rupture in the Pacific Plate. *Geophysical Research Letters*, *45*(18), 9542–9551. Retrieved 2023-01-18, from https://onlinelibrary.wiley.com/doi/10.1029/2018GL079813 doi: 10.1029/2018GL079813

Mai, P. M., & Thingbaijam, K. K. S. (2014, November). SRCMOD: An Online Database of Finite-Fault Rupture Models. *Seismological Research Letters*, *85*(6), 1348–1357. Retrieved 2023-01-13, from https://pubs.geoscienceworld.org/

srl/article/85/6/1348-1357/315623 doi: 10.1785/0220140077

McGuire, J. J. (2002, December). Predominance of Unilateral Rupture for a Global Catalog of Large Earthquakes. *Bulletin of the Seismological Society of America*, *92*(8), 3309–3317. Retrieved 2020-11-05, from https://pubs.geoscienceworld.org/bssa/article/92/8/3309-3317/103071 doi: 10.1785/0120010293

McGuire, J. J. (2004, April). Estimating Finite Source Properties of Small Earthquake Ruptures. *Bulletin of the Seismological Society of America*, *94*(2), 377–393. Retrieved 2020-11-05, from https://pubs.geoscienceworld.org/bssa/article/94/2/377-393/146918 doi: 10.1785/0120030091

McGuire, J. J., & Beroza, G. C. (2012, June). A Rogue Earthquake Off Sumatra. *Science*, *336*(6085), 1118–1119. Retrieved 2023-01-18, from https://www.science.org/doi/10.1126/science.1223983 doi: 10.1126/science.1223983

McGuire, J. J., Zhao, L., & Jordan, T. H. (2000, August). Rupture dimensions of the 1998 Antarctic Earthquake from low-frequency waves. *Geophysical Research Letters*, *27*(15), 2305–2308. Retrieved 2020-11-05, from http://doi.wiley.com/10.1029/1999GL011186 doi: 10.1029/1999GL011186

McGuire, J. J., Zhao, L., & Jordan, T. H. (2001, June). Teleseismic inversion for the second-degree moments of earthquake space-time distributions. *Geophysical Journal International*, *145*(3), 661–678. Retrieved 2020-11-05, from https://academic.oup.com/gji/article-lookup/doi/10.1046/j.1365-246x.2001.01414.x doi: 10.1046/j.1365-246x.2001.01414.x

Meng, H., McGuire, J. J., & Ben-Zion, Y. (2020, April). Semiautomated estimates of directivity and related source properties of small to moderate Southern California earthquakes using second seismic moments. *Journal of Geophysical Research: Solid Earth*, *125*(4), e2019JB018566. Retrieved 2021-06-23, from https://onlinelibrary.wiley.com/doi/10.1029/2019JB018566 doi: 10.1029/2019JB018566

Meng, L., Ampuero, J.-P., Stock, J., Duputel, Z., Luo, Y., & Tsai, V. C. (2012, August). Earthquake in a Maze: Compressional Rupture Branching During the 2012 $M_w$ 8.6 Sumatra Earthquake. *Science*, *337*(6095), 724–726. Retrieved 2023-01-13, from https://www.science.org/doi/10.1126/science.1224030 doi: 10.1126/science.1224030

Moulik, P., & Ekström, G. (2014, December). An anisotropic shear velocity model of the Earth's mantle using normal modes, body waves, surface waves and long-period waveforms. *Geophysical Journal International*, *199*(3), 1713–1738. Retrieved 2021-11-04, from http://academic.oup.com/gji/article/199/3/1713/617840/An-anisotropic-shear-velocity-model-of-the-Earths doi: 10.1093/gji/ggu356

Nettles, M., Wallace, T. C., & Beck, S. L. (1999, July). The March 25, 1998 Antarctic Plate Earthquake. *Geophysical Research Letters*, *26*(14), 2097–2100. Retrieved 2023-01-13, from http://doi.wiley.com/10.1029/1999GL900387 doi: 10.1029/1999GL900387

Reilinger, R. E., Ergintav, S., Bürgmann, R., McClusky, S., Lenk, O., Barka, A., ... Töksoz, M. N. (2000, September). Coseismic and Postseismic Fault Slip for the 17 August 1999, M = 7.5, Izmit, Turkey Earthquake. *Science*, *289*(5484), 1519–1524. Retrieved 2023-01-19, from https://www.science.org/doi/10.1126/science.289.5484.1519 doi: 10.1126/science.289.5484.1519

Robinson, D. P. (2011, September). A rare great earthquake on an oceanic fossil fracture zone: The 2004 Tasman Sea earthquake. *Geophysical Journal International*, *186*(3), 1121–1134. Retrieved 2023-01-18, from https://academic.oup.com/gji/article-lookup/doi/10.1111/j.1365-246X.2011.05092.x doi: 10.1111/j.1365-246X.2011.05092.x

Ross, Z. E., Trugman, D. T., Azizzadenesheli, K., & Anandkumar, A. (2020, February). Directivity Modes of Earthquake Populations with Unsupervised Learning.

*Journal of Geophysical Research: Solid Earth*, *125*(2). Retrieved 2023-03-09, from https://onlinelibrary.wiley.com/doi/abs/10.1029/2019JB018299 doi: 10.1029/2019JB018299

Scripps Institution Of Oceanography. (1986). *IRIS/IDA Seismic Network.* International Federation of Digital Seismograph Networks. Retrieved from http://www.fdsn.org/doi/10.7914/SN/II doi: 10.7914/SN/II

Seton, M., Müller, R. D., Zahirovic, S., Williams, S., Wright, N. M., Cannon, J., ... McGirr, R. (2020, October). A Global Data Set of Present-Day Oceanic Crustal Age and Seafloor Spreading Parameters. *Geochemistry, Geophysics, Geosystems*, *21*(10). Retrieved 2023-02-22, from https://onlinelibrary.wiley.com/doi/10.1029/2020GC009214 doi: 10.1029/2020GC009214

Seton, M., Whittaker, J. M., Wessel, P., Müller, R. D., DeMets, C., Merkouriev, S., ... Williams, S. E. (2014, April). Community infrastructure and repository for marine magnetic identifications. *Geochemistry, Geophysics, Geosystems*, *15*(4), 1629–1641. Retrieved 2022-12-08, from http://doi.wiley.com/10.1002/2013GC005176 doi: 10.1002/2013GC005176

Silver, P. G., & Jordan, T. H. (1983). Total-moment spectra of fourteen large earthquakes. *Journal of Geophysical Research*, *88*(B4), 3273. Retrieved 2020-11-05, from http://doi.wiley.com/10.1029/JB088iB04p03273 doi: 10.1029/JB088iB04p03273

Socquet, A., Hollingsworth, J., Pathier, E., & Bouchon, M. (2019, March). Evidence of supershear during the 2018 magnitude 7.5 Palu earthquake from space geodesy. *Nature Geoscience*, *12*(3), 192–199. Retrieved 2023-01-19, from http://www.nature.com/articles/s41561-018-0296-0 doi: 10.1038/s41561-018-0296-0

Wesnousky, S. G. (2008, August). Displacement and Geometrical Characteristics of Earthquake Surface Ruptures: Issues and Implications for Seismic-Hazard Analysis and the Process of Earthquake Rupture. *Bulletin of the Seismological Society of America*, *98*(4), 1609–1632. Retrieved 2022-01-10, from https://pubs.geoscienceworld.org/bssa/article/98/4/1609-1632/350111 doi: 10.1785/0120070111

Wessel, P., Luis, J. F., Uieda, L., Scharroo, R., Wobbe, F., Smith, W. H. F., & Tian, D. (2019). *The generic mapping tools.* Retrieved from https://www.generic-mapping-tools.org/

Wessel, P., Matthews, K. J., Müller, R. D., Mazzoni, A., Whittaker, J. M., Myhill, R., & Chandler, M. T. (2015, July). Semiautomatic fracture zone tracking: SEMI-AUTOMATIC FRACTURE ZONE TRACKING. *Geochemistry, Geophysics, Geosystems*, *16*(7), 2462–2472. Retrieved 2022-12-08, from http://doi.wiley.com/10.1002/2015GC005853 doi: 10.1002/2015GC005853

Wiens, D. A., & Stein, S. (1983). Age dependence of oceanic intraplate seismicity and implications for lithospheric evolution. *Journal of Geophysical Research*, *88*(B8), 6455. Retrieved 2023-01-18, from http://doi.wiley.com/10.1029/JB088iB08p06455 doi: 10.1029/JB088iB08p06455

Yin, J., Li, Z., & Denolle, M. A. (2021). Source Time Function Clustering Reveals Patterns in Earthquake Dynamics. , *92*(4).

Çakir, Z., Chabalier, J.-B. d., Armijo, R., Meyer, B., Barka, A., & Peltzer, G. (2003, October). Coseismic and early post-seismic slip associated with the 1999 Izmit earthquake (Turkey), from SAR interferometry and tectonic field observations. *Geophysical Journal International*, *155*(1), 93–110. Retrieved 2023-01-19, from https://academic.oup.com/gji/article-lookup/doi/10.1046/j.1365-246X.2003.02001.x doi: 10.1046/j.1365-246X.2003.02001.x